Feasibility of an innovative amorphous silicon photovoltaic/thermal system for medium temperature applications

Xiao Ren[a]

Jing Li[b, *]

lijing83@ustc.edu.cn

Mingke Hu[a]

Gang Pei[a, *]

peigang@ustc.edu.cn

Dongsheng Jiao[a]

Xudong Zhao[b]

Jie Ji[a]

[a]Department of Thermal Science and Energy Engineering, University of Science and Technology of China, 96 Jinzhai Road, Hefei, China

[b]School of Engineering and Computer Science, University of Hull, Hull HU6 7RX, UK

*Corresponding authors.

Abstract

Medium temperature photovoltaic/thermal (PV/T) systems have immense potential in the applications of absorption cooling, thermoelectric generation, and organic Rankine cycle power generation, etc. Amorphous silicon (a-Si) cells are promising in such applications regarding the low temperature coefficient, thermal annealing effect, thin film and avoidance of large thermal stress and breakdown at fluctuating temperatures. However, experimental study on the a-Si PV/T system is rarely reported. So far the feasibility of medium temperature PV/T systems using a-Si cells has not been demonstrated. In this study, the design and construction of an innovative a-Si PV/T system of stainless steel substrate are presented. Long-term outdoor performance of the system operating at medium temperature has been monitored in the past 15 months. The average electrical efficiency was 5.65%, 5.41% and 5.30% at the initial, intermediate and final phases of the long-test test, accompanied with a daily average thermal efficiency from about 21% to 31% in the non-heating season. The thermal and electrical performance of the system at 60 °C, 70 °C and 80 °C are also analyzed and compared. Moreover, a distributed parameter model with experimental validation is developed for an inside view of the heat transfer and power generation and to predict the system performance in various conditions. Technically, medium temperature operation has not resulted in interruption or observable deformation of the a-Si PV/T system during the period. The technical and thermodynamic feasibility of the a-Si PV/T system at medium operating temperature is demonstrated by the experimental and simulation results.

Keywords: Amorphous silicon cells; Photovoltaic/thermal; Medium temperature; Long-term test; Feasibility

Nomenclature

A

area, m^2

B

temperature coefficient, K^{-1}

c

specific heat capacity, J/kg K

d

thickness, m

D

diameter, m

E

electrical gain

G

solar irradiation, W/m^2

h

heat transfer coefficient, W/m^2 K

H

total solar radiation MJ/m^2; J/m^2

I

current, A

$\dot{m}$

mass flow rate, kg/s

$\dot{M}$

mass flow rate, kg/s

Nu

Nusselt number, –

P

perimeter, m

Q

energy, W; kWh

R

thermal resistance, K/W

Ra

Raleigh number, –

t

time, s

T

temperature, K

u

flow velocity, m/s

U

voltage, V

Greek letters

α

absorptivity, –

β

slope angle of collector, °

θ

incidence angle, °

ϕ

latitude, °

ω

hour angle of the sun, °

γ

surface azimuth angle, °

δ

declination angle of the sun, °

ε

emissivity, –

η

efficiency, –

$(\tau\alpha)_{\mathrm{pv}}$

effective absorption, –

ξ

covering factor, –

λ

thermal conduction, W/m K

ρ

density, kg/m^3

ρ_d

reflection of glass cover, –

σ

Stefan-Boltzman constant, W/m^2 K^4

τ

transmittance, –

Subscripts

a

ambient, air

ad

adhesive layer

b

absorber plate

bt

welding layer

c

collector

e

sky

g

glass

il

insulation layer

in

inlet of collector

mp

maximum power

out

outlet of collector

pv

PV module

ref

standard test condition

t

copper tube

TPT

black TPT

w

water

1 Introduction

Hybrid photovoltaic/thermal (PV/T) collectors represent the integration of solar thermal collectors and photovoltaic (PV) modules and exhibit higher efficiency in solar energy utilization. The primary purposes of PV/T systems are to reduce the operation temperature and recover the excess heat released by PV cells [1]. Thermal energy is regarded as a secondary benefit of PV/T systems, which is mainly used in the low temperature applications such as domestic hot water and space heating.

Recently medium temperature PV/T systems have been attracting increasing attention. The potential applications of these systems include PV/T-absorption cooling [2], PV/T-thermoelectric generation [3], and hybrid PV/T and organic Rankine cycle (PV/T-ORC) power generation [4]. Most solar cooling systems usually use hot water driven lithium bromide absorption chillers. The driving temperature for absorption chillers is in the range of 75–90 °C. The PV/T cooling system can cover a significant percentage of the domestic heating and cooling demands [5], and can serve as a highly competitive solar cooling solution [6,7]. A PV/T-thermoelectric system combining the PV/T collectors and thermoelectric generators enhances the thermal stability of the system's electrical efficiency [8] and increases the total energy yields [9]. A PV/T-ORC system takes advantage of the PV and ORC technologies [10,11] and can use thermal storage e.g. water instead of battery for flexible power generation [12,13].

The selection of solar cells is crucial for the viability and performance of the PV/T system at medium temperature. Mainstream PV/T systems use crystalline silicon (c-Si) cells as PV materials. However, some characteristics of c-Si cells tend to limit the development and application of PV/T collectors in the medium temperature field. On the one hand, c-Si cells exhibit higher power temperature coefficients at maximum power point of about −0.41 to −0.5%/°C, and the electrical efficiency decreases significantly as the temperature rises. The temperature of PV module strongly affects the electrical performance, whereas the ambient temperature and the solar radiation are the two main factors that influence the temperature of PV module [14]. As described in the study by Radziemska [15], when the operating temperature increased from 25 °C to 60 °C, the maximum output power decreased from 79.60 W to 61.28 W and the electrical efficiency decreased from 13.3% to 10.3%. In the extreme case, the PV/T systems lack advantage over side-by-side PV and solar collector systems. On the other hand, PV modules are usually laminated on an aluminum plate to ensure good thermal conductivity, and the coefficient of the thermal expansion of aluminum at 20 °C is about 23×10^{-6}/°C, which is significantly higher than the value of c-Si cells (about 2.6×10^{-6}/°C) [16]. Large temperature difference between the working fluid and the PV module in PV/T collector may cause rapid and inhomogeneous thermal contraction and large thermal stresses [17,18]. High levels of thermal stress may lead to the permanent structural damage of the PV cells [19], and an example is shown in Fig. 1 [20]. The tendency of c-Si PV/T collectors to break easily under long-term operation due to the gradient and fluctuation of temperature (e.g., abruption and deformation) is a serious technical problem. c-Si components are susceptible to cracking due to the nature of their crystal structure. In particular, the ability of the thin c-Si cells to prevent mechanical damage is reduced, and micro-cracks are more prone to occur [21].

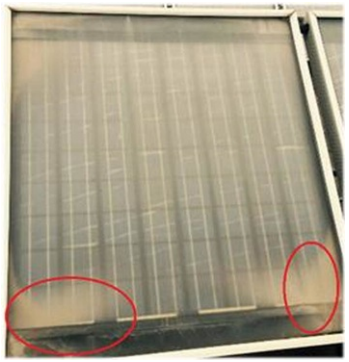

Fig. 1 A broken c-Si PV/T collector.

Fortunately, amorphous silicon (a-Si) cells as materials of PV/T collectors provide a promising solution. Although a-Si cells as PV materials receive less attention than c-Si cells in PV/T applications, several studies have explored the other applications of a-Si cells, such as PV windows [22], semi-transparent PV façade [23,24], building integrated PV systems [25], PV walls [26], and thermoelectric-PV systems [27,28]. The following characteristics make a-Si cells highly suitable for operating at medium temperature.

First, the power temperature coefficient of a-Si cells varies from −0.1 to −0.2%/°C in a short time range of several hours; thereby a-Si cells are more suitable for operating at medium temperature without substantial power loss [29]. Studies have also shown that the power temperature coefficients of a-Si cells exhibited positive in a long time test [30,31].

Second, thin-film a-Si cells are flexible and can be easily deposited onto a stainless steel sheet and glass at low temperature. The characteristic of thin-film not only makes a-Si cells reduce the use of silicon materials, but also presents lower thermal resistance than c-Si cells. Moreover, a-Si cells can avoid huge thermal stress and overcome the problem of interruptions at fluctuating temperatures in PV/T collectors.

Third, compared with that of c-Si cells, the electrical efficiency of a-Si cells is not high at room temperature; nevertheless, a-Si cells are able to benefit from thermal annealing at high operating temperature and reduce defect states, leading to an improvement of electrical performance [32]. Experiments have demonstrated that a-Si cells gained high energy output from high-temperature operations and thermal annealing at 100 °C for 1 h on a 12 h cycle [33]. The degradation during cold soaking (22 ± 8 °C) at 1-sun for about 1000 h could be restored upon subsequent warm soaking (51 ± 8 °C) for several hundred hours, resulting in an increase in electrical efficiency from 10% to 17% [34]. Therefore, a-Si cells are expected to exhibit high electrical efficiency at high temperatures.

Although the mainstream a-Si cells on the market have a relatively low efficiency, improved performance can be expected in the future. For instance, an initial cell efficiency of 14.6% for a-Si solar cells has been obtained by United Solar Systems Corporation [35], and a cell efficiency of up to 12.7% for triple-junction a-Si cells has been demonstrated by the University of Toledo [36], and a-Si cells deposited on doped LPCVD-ZnO can reach a stabilized cell efficiency of 10.09% [37]. The above characteristics suggest that a-Si cells are a promising choice as PV materials for PV/T collectors used in the fields of medium temperature.

Several theoretical studies on a-Si PV/T systems have been reported at medium temperature. For example, the effects of high-temperature annealing and the thickness of intrinsic layers on a-Si cells were investigated in a hybrid PV/T collector [33,38], and an annealing model for a-Si cells was developed to study the optimization of the dispatch strategy and then applied to different regions [39]. Some other theoretical studies on a-Si PV/T systems were performed at low operating temperature. Kalogirou et al. [40] presented TRNSYS simulation results for hybrid PV/T solar systems made from polycrystalline silicon cells and a-Si cells for domestic hot water applications. Kanchan et al. [41] evaluated the energy and exergy performance of a building integrated semitransparent PV/T system using a-Si cells. Simulation studies on a-Si and c-Si PV/T systems were carried out in steady state, and the results showed that the electrical efficiencies of a-Si and c-Si cells each were 4.9% and 11.6% [42]. In these studies, the lumped parameter model was generally adopted, which assumed that the temperature difference inside the model (absorber, PV cells, glass cover, water tube, etc.) was negligible. It is difficult to accurately predict the system behaviour at medium temperature and reveal the mechanism of heat transfer and power conversion inside PV/T modules.

There have been a few experimental studies on the a-Si PV/T systems. The field tests of PV/T systems using a-Si cells for residential application have been done in Bangkok, with the average thermal efficiency of 51% and electricity efficiency of 4.0% [43]. Investigation on a heat pipe a-Si PV/T system has been done in Changsha, China, with an average electricity efficiency of 4.8% and thermal efficiency of 41% [44]. In the authors' previous work [45], a PV/T system using a-Si cells deposited on stainless steel was tested for the first time. Preliminary outdoor experiments in the temperature range from about 20 to 50 °C were conducted. Notably, these experimental studies were carried out at low operating temperature. Medium temperature experiment on a-Si PV/T system is rarely reported.

Though medium temperature PV/T systems have excellent and widespread application prospect and a-Si cells are a promising choice as the PV materials, the practical use is lacked. The feasibility has not been demonstrated

yet. Stainless steel offers better thermal conduction than conventional substrates i.e. glass and plastic, but might easily incur electrical conduction to the metal absorber after long term operation, leading to failure in power generation. The lifetime of the a-Si PV/T system in the medium temperature application is unknown. Both the technical and thermodynamic issues need to be clarified.

To fill the above knowledge gaps of a-Si PV/T system, the design and construction of a novel standard sized PV/T using a-Si cells deposited on stainless steel are introduced in this paper. Experiment results on the long-term behavior of a-Si PV/T system at medium operating temperature are presented. The performances of the system at 60 °C, 70 °C, and 80 °C are also analyzed and compared. A distributed parameter model is also established for a better understanding of the heat transfer and power generation and to analyze the system behavior in both heating and non-heating period. Finally, the technical and thermodynamic feasibility is demonstrated.

2 Description of the a-Si PV/T system and experimental setup

2.1 Description of the a-Si PV/T collector

In the authors' previous work at low operating temperature [45], the constructed collector (1100 mm × 820 mm) was designed to be smaller than a common c-Si PV/T collector to reduce the risk of electric conduction between the stainless steel and aluminum absorber. The thermal performance of the first prototype was expected to be low due to its small size.

Following the success of the first prototype, a new a-Si PV/T system with a standard dimension of 1950 mm × 950 mm was further developed with enhanced thermal and electrical performance. The structure of the new a-Si PV/T collector is presented in Fig. 2. The a-Si PV/T collector consists of the following components: glass cover, a-Si cell, aluminum absorber plate, copper tube, and insulation layer. Fifteen pieces of a-Si cells are laminated onto the absorber plate through the adhesive layer (black TPT and EVA), in which the area of a single a-Si cell is 356 mm × 239 mm. The PV characteristics of a piece of a-Si cell at standard test conditions (temperature of 25 °C and solar radiation of 1000 W/m^2) are given as follows: the voltage, current, and power at the maximum power point each are 1.6 V, 4.1 A, and 6.5 W. The transparent TPT and EVA are employed to encapsulate and protect the a-Si cells. A piece of absorber plate with an area of 1950 mm × 950 mm is used as the base panel. The back of the absorber plate has seven copper tubes and two header pipes. The length and diameter of each copper tube are 1900 and 8 mm, and the distance between two copper tubes is 135 mm. Two water collector pipes in the upper and lower parts of the back of the absorber plate are 1060 and 22 mm in the length and diameter. To reduce the heat loss, an insulation layer is employed on the bottom of the a-Si PV/T collector.

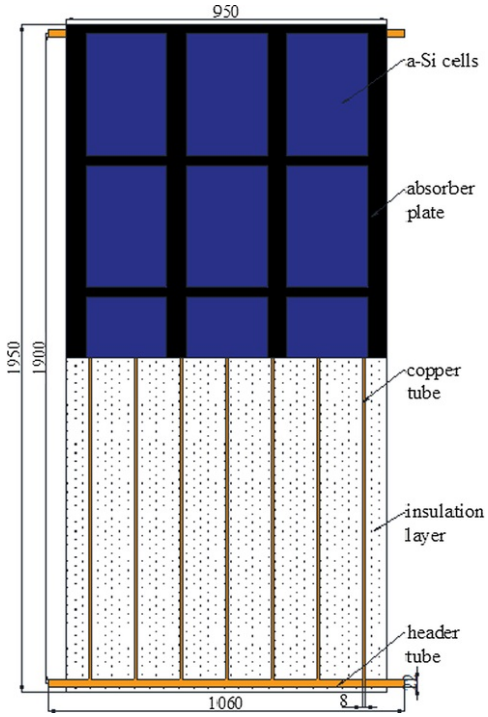

Fig. 2 Structure and dimensions of the a-Si PV/T collector.

2.2 Experimental setup

To evaluate the medium temperature performance of the a-Si PV/T system, the experiment system was constructed, as shown in Fig. 3. The collector was installed southward in Hefei, China (117.15°E and 34.27°N) with a slope angle of 30° to maximize solar radiation obtained by the collector [46]. As shown in Fig. 4, the experiment system is primarily composed of an a-Si PV/T collector, a water circulation system (the red line) and an electrical connection system (the blue[1] line). The water circulation system includes a thermostatic water tank and a turbine flowmeter. In the electrical connection system, a maximum power point tracking solar charge controller is employed to track the current and voltage of the maximum power point. The generated electrical energy can be stored in the solar battery or consumed by the DC load. The types of the experimental measurement instruments are presented in Table 1.The slope angle of the radiometer is the same as the slope angle of the collector to measure the total solar radiation (direct and diffuse radiation) on the collector surface. As the green line shown in the Fig. 4, all data are recorded and stored by the Agilent Bench Link Data Logger (34980A) with a time internal of 10 s.

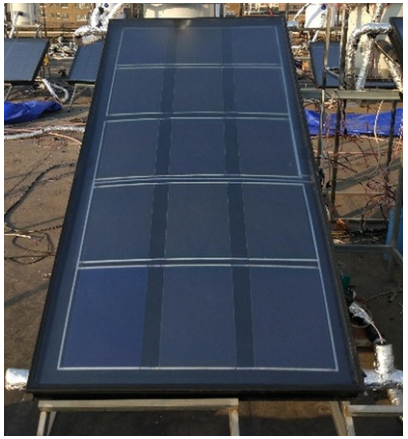

Fig. 3 Actual setup of the a-Si PV/T system test rig.

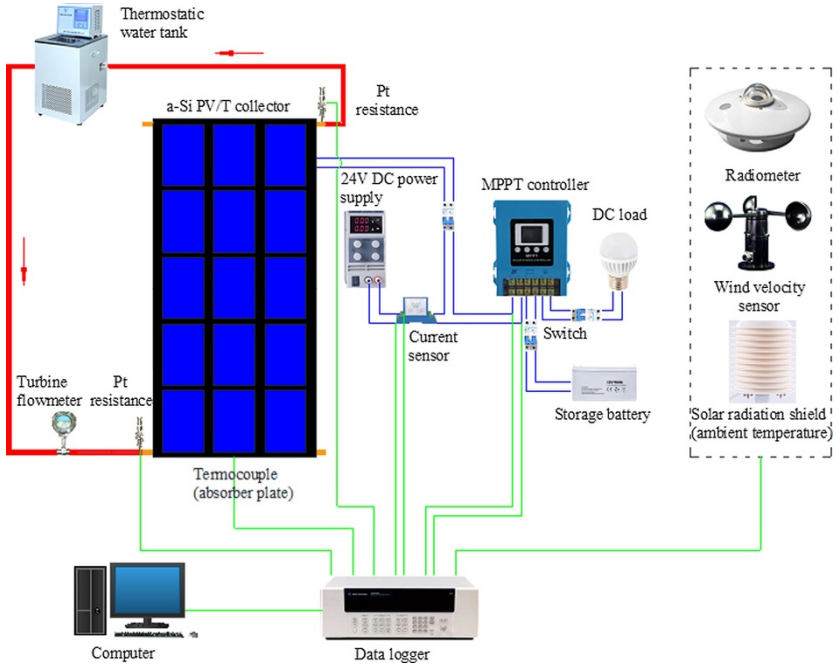

Fig. 4 Schematic diagram of the a-Si PV/T system test rig.

Table 1 Types of experimental measurement instruments.

Instruments	Types	Uncertainty	Location
Platinum resistance	Pt 100	±0.1 °C	Inlet and outlet of collector
Thermocouple	Type T	±0.5 °C	Ambient; absorber plate
Flowmeter	LWGY	±5%	Outlet of the thermostatic water tank
Current sensor	HKK-13-I	±0.1%	PV module output circuit
Radiometer	TBQ-2	±2%	Solar collector

3 Mathematical model and simulation

In this part, a distributed parameter model is established to study the performance of the a-Si PV/T system. The cross section and heat transfer process of the a-Si PV/T collector are shown in Fig. 5. The a-Si PV/T system consists of the following parts: incidence angle of solar radiation, glass cover, PV module, absorber plate, copper tube, and flowing water in copper tube. The following assumptions are made to simplify the analysis [47]:

(1) The water flow rate in each copper tube is uniform. Hence, the temperature of the absorber plate is assumed to be symmetrically distributed along the axial direction of each copper tube.

(2) The temperature gradients of the glass cover, PV module, absorber plate, and copper pipe along the thickness direction are negligible.

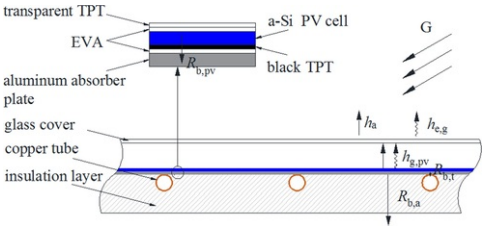

Fig. 5 Cross section and heat transfer process of the a-Si PV/T collector.

3.1 Modeling of the incidence angle of solar radiation on the collector surface

The angle of incidence of solar radiation on the collector surface is defined as [48]

$$\begin{aligned}\cos\theta = {} & \sin\delta(\sin\phi\cos\beta - \cos\phi\sin\beta\cos\gamma) + \cos\delta\cos\omega\cos\phi\cos\beta \\ & + \cos\delta\cos\omega\sin\phi\sin\beta\cos\gamma + \cos\delta\sin\beta\sin\gamma\sin\omega\end{aligned} \tag{1}$$

where θ is the incidence angle of solar radiation on collector surface (°); ϕ is the latitude of the collector (°); ω is the hour angle of the sun (°); γ is the surface azimuth angle of the collector, with zero due south, positive due west, and negative due east (°); and δ is the declination angle of the sun (°).

The PV/T collector is facing south, and thus, the incidence angle can be simplified as

$$\cos\theta = \sin\delta\sin(\phi-\beta) + \cos\delta\cos\omega\cos(\phi-\beta) \tag{2}$$

3.2 Modeling of glass cover

The energy balance equation of the glass cover can be expressed as

$$\rho_g c_g d_g \frac{\partial T_g}{\partial t} = h_a(T_a - T_g) + h_{e,g}(T_e - T_g) + h_{g,pv}(T_{pv} - T_g) + G\alpha_g \tag{3}$$

where $h_{e,g}$ is the radiant heat transfer coefficient between the glass cover and sky; $h_{g,pv}$ is the heat transfer coefficient between the glass cover and a-Si cells combines convection and radiation, expressed as

$$\begin{aligned}h_{g,pv} = {} & \sigma(T_{pv}^2 + T_g^2)(T_{pv} + T_g)\left(\frac{\xi}{1/\varepsilon_{pv}+\xi(1/\varepsilon_g-1)} + \frac{1-\xi}{1/\varepsilon_{pv}+(1-\xi)(1/\varepsilon_g-1)}\right) \\ & + \frac{Nu\cdot\lambda_a}{d_a}\end{aligned} \tag{4}$$

where ξ is the covering factor of PV cells and is defined as

$$\xi = A_{pv}/A_c \tag{5}$$

For the tilt angle of the collector within 0° to 75°, the Nusselt number is expressed as [49]

$$Nu = 1 + 1.14\left(1 - \frac{1708(\sin 1.8\beta)^{1.6}}{Ra\cdot\cos\beta}\right)\left[1 - \frac{1708}{Ra\cdot\cos\beta}\right]^+ + \left[\left(\frac{Ra\cdot\cos\beta}{5830}\right)^{1/3} - 1\right]^+ \tag{6}$$

where $[]^+$ indicates that only positive values for the terms in the square brackets are used; in case of negative values, zero is used.

3.3 Modeling of PV module

The two-dimensional energy balance equation for the PV module is expressed as

$$\begin{aligned}\rho_{pv}c_{pv}d_{pv}\frac{\partial T_{pv}}{\partial t} = {} & \lambda_{pv}d_{pv}\left(\frac{\partial^2 T_{pv}}{\partial x^2} + \frac{\partial^2 T_{pv}}{\partial y^2}\right) + h_{g,pv}\left(T_g - T_{pv}\right) + \left(T_b - T_{pv}\right)/R_{b,pv} \\ & + G(\tau\alpha)_{pv} - \xi E_{pv}\end{aligned} \tag{7}$$

The effective absorption $(\tau\alpha)_{pv}$ and output power E_{pv} of the PV module are respectively expressed as

$$(\tau\alpha)_{\mathrm{pv}} = \frac{\tau_{\mathrm{g}}\tau_{\mathrm{ad}}\alpha}{1-(1-\alpha)\rho_{\mathrm{d}}} \tag{8}$$

$$E_{\mathrm{pv}} = G\tau_{\mathrm{g}}\tau_{\mathrm{ad}}\eta_{\mathrm{ref}}\left[1-B_r\left(T_{\mathrm{pv}}-T_{\mathrm{ref}}\right)\right] \tag{9}$$

where τ_{g} and τ_{ad} are the transmittances of the glass cover and adhesive (transparent TPT and EVA); ρ_{d} is the reflection of the glass cover to the diffuse radiation; η_{ref} is the electrical efficiency of the PV cells under standard test conditions (%); $T_{\mathrm{ref}} = 298.15\,\mathrm{K}$ is the temperature of the standard test condition; B_{r} is the temperature coefficient (K^{-1}); α is the comprehensive absorption given by the weighted average of the absorptions of black TPT (α_{TPT}) and PV cells (α_{pv}) and expressed as

$$\alpha = \xi\alpha_{\mathrm{pv}} + (1-\xi)\,\alpha_{\mathrm{TPT}} \tag{10}$$

$R_{\mathrm{b,pv}}$ is the thermal resistance of the adhesive layer (black TPT and EVA) between the absorber plate and PV module ($\mathrm{m}^2\,\mathrm{K/W}$) and is expressed as

$$R_{\mathrm{b,pv}} = \frac{d_{\mathrm{ad}}}{\lambda_{\mathrm{ad}}} \tag{11}$$

3.4 Modeling of absorber plate

For the absorber plate, two types of energy balance equations are considered. One type is for nodes welded with the copper tubes and has direct heat conduction with the copper tubes (connection nodes). The other type is for the part between the copper tubes (middle nodes).

The energy balance equation of the connection nodes is given as

$$\rho_{\mathrm{b}}c_{\mathrm{b}}d_{\mathrm{b}}\frac{\partial T_{\mathrm{b}}}{\partial t} = \lambda_{\mathrm{b}}d_{\mathrm{b}}\left(\frac{\partial^2 T_{\mathrm{b}}}{\partial x^2}+\frac{\partial^2 T_{\mathrm{b}}}{\partial y^2}\right) + \left(T_{\mathrm{pv}}-T_{\mathrm{b}}\right)/R_{\mathrm{b,pv}} + \frac{T_{\mathrm{t}}-T_{\mathrm{b}}}{R_{\mathrm{b,t}}\cdot A_{ij}} \tag{12}$$

The energy balance equation of the middle nodes is given as

$$\rho_{\mathrm{b}}c_{\mathrm{b}}d_{\mathrm{b}}\frac{\partial T_{\mathrm{b}}}{\partial t} = \lambda_{\mathrm{b}}d_{\mathrm{b}}\left(\frac{\partial^2 T_{\mathrm{b}}}{\partial x^2}+\frac{\partial^2 T_{\mathrm{b}}}{\partial y^2}\right) + \left(T_{\mathrm{pv}}-T_{\mathrm{b}}\right)/R_{\mathrm{b,pv}} + \left(T_{\mathrm{a}}-T_{\mathrm{b}}\right)/R_{\mathrm{b,a}} \tag{13}$$

where A_{ij} is the area of a single controller (m^2).

The thermal resistance $R_{\mathrm{b,a}}$ ($\mathrm{m}^2\cdot\mathrm{K/W}$) between the absorber plate and ambient air is written as

$$R_{\mathrm{b,a}} = d_{\mathrm{il}}/\lambda_{\mathrm{il}} + 1/h_{\mathrm{a}} \tag{14}$$

The thermal resistance $R_{\mathrm{b,t}}$ (K/W) between the absorber plate and copper pipe is expressed as

$$R_{\mathrm{b,t}} = d_{\mathrm{bt}}/\left(\lambda_{\mathrm{bt}}\cdot A_{\mathrm{bt}}\right) \tag{15}$$

where A_{bt} is the welding area in a single controller (m^2).

3.5 Modeling of copper tube

The energy balance equation of the copper tube is expressed as

$$A_{\mathrm{t}}\rho_{\mathrm{t}}c_{\mathrm{t}}\frac{\partial T_{\mathrm{t}}}{\partial t} = A_{\mathrm{t}}\lambda_{\mathrm{t}}\frac{\partial^2 T_{\mathrm{t}}}{\partial x^2} + \pi D_{\mathrm{t}}h_{\mathrm{w,t}}(T_{\mathrm{w}}-T_{\mathrm{t}}) + \frac{T_{\mathrm{b}}-T_{\mathrm{t}}}{R_{\mathrm{b,t}}\cdot dx} \tag{16}$$

where $h_{\mathrm{w,t}}$ is the convective heat transfer coefficient between the copper tube and water flow ($\mathrm{W/(m^2\,K)}$).

3.6 Modeling of water flow

For the water flowing in the copper tube, the energy balance equation is expressed as

$$A_{\mathrm{w}}\rho_{\mathrm{w}}c_{\mathrm{w}}\frac{\partial T_{\mathrm{w}}}{\partial t} = -\dot{m}c_{\mathrm{w}}\frac{\partial T_{\mathrm{w}}}{\partial x} + A_{\mathrm{w}}\lambda_{\mathrm{w}}\frac{\partial^2 T_{\mathrm{w}}}{\partial x^2} + P_{\mathrm{w}}h_{\mathrm{w,t}}\left(T_{\mathrm{t}}-T_{\mathrm{w}}\right) \tag{17}$$

where $\dot{m}$ is the mass flowing rate of the water in a single copper tube (kg/s); A_t and P_t are the cross-sectional area (m^2) and perimeter of the runner in the copper tube (m).

3.7 Performance evaluation

The instantaneous thermal efficiency of the collector can be defined as

$$\eta_{th} = \frac{\dot{M}c_w\left(T_{out} - T_{in}\right)}{GA_c} \tag{18}$$

where $\dot{M}$ is the mass flowing rate of the water in collector (kg/s); T_{out} and T_{in} are the outlet and inlet temperatures of the collector (K).

To combine the effect of ambient temperature, solar radiation and inlet temperature, and to get general conclusions, a linear correlation between the instantaneous thermal efficiency and the reduced temperature $(T_{in} - T_a)/G$ is built, expressed as [50]:

$$\eta_{th} = F_R(\tau\alpha)_e - F_R U_L \frac{T_{in} - T_a}{G} \tag{19}$$

The intercept $F_R(\tau\alpha)_e$ and slope $F_R U_L$ are the thermal efficiency at zero reduced temperature and the heat loss of the collector.

The electrical efficiency is defined as ratio of the electrical power to the incident solar radiation

$$\eta_{pv} = \frac{E_{pv}}{GA_{pv}} \tag{20}$$

For the simulation, the electrical power is calculated by Eq.(9), while the experimental electrical power is expressed as:

$$E_{pv} = U_{mp}I_{mp} \tag{21}$$

To evaluate the degree of agreement between the simulation and the experimental results, mean relative error (MRE) is defined as

$$MRE = \frac{\sum_{i=1}^{i=N}\left|X_{exp} - X_{sim}\right|}{\sum_{i=1}^{i=N}X_{exp}} \times 100\% \tag{22}$$

where X_{exp} and X_{sim} are the experimental and simulation results, respectively.

4 Discretization of equations and numerical simulation

The x-axis refers to the direction along the copper tube, and the y-axis is along the direction of the header tube. The temperature of absorber plate is distributed symmetrically along the axial direction of each copper tube, hence half area between two copper tubes with symmetric boundary conditions on both sides in y-axis is selected to solve the energy balance equations of absorber plate and PV module. The two-dimensional discrete nodes ($i \times j = 51 \times 11$) of the PV module and absorber plate are shown in the Fig. 6. For the copper tube and the water in it, 49×1 nodes are established for grid discretization.

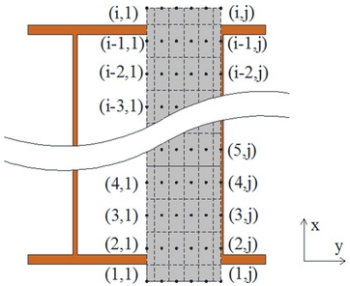

Fig. 6 Differential grid partition of PV module and absorber plate.

All the energy balance equations of the unsteady state model are solved by a fully implicit scheme, in which the energy balance equations of the PV module, absorber plate, and copper tube are discretized by a second-order

central difference scheme; the energy balance equation of the water in copper tube is discretized by a second-order windward scheme. The distributed parameter model of the a-Si PV/T system can be discretized as follows.

For the glass cover:

$$\rho_g c_g d_g (T_g^1 - T_g^0) = h_a (T_a - T_g^1) + h_{e,g} (T_e - T_g^1) + h_{g,pv} (T_{pv}^1 - T_g^1) + G\alpha_g \tag{23}$$

For the PV module:

$$\begin{aligned} \rho_{pv} c_{pv} d_{pv} \frac{T_{pv(i,j)}^1 - T_{pv(i,j)}^0}{\Delta t} &= \lambda_{pv} d_{pv} \frac{T_{pv(i+1,j)}^1 - 2T_{pv(i,j)}^1 + T_{pv(i-1,j)}^1}{\Delta x^2} \\ &+ \lambda_{pv} d_{pv} \frac{T_{pv(i,j+1)}^1 - 2T_{pv(i,j)}^1 + T_{pv(i,j-1)}^1}{\Delta y^2} \\ + h_{g,pv} \left(T_g^1 - T_{pv(i,j)}^1 \right) + \frac{T_{b(i,j)}^1 - T_{pv(i,j)}^1}{R_{b,pv}} &+ G(\tau\alpha)_{pv} - \xi E_{pv} \end{aligned} \tag{24}$$

For the middle nodes of the absorber plate:

$$\begin{aligned} \rho_b c_b d_b \frac{T_{b(i,j)}^1 - T_{b(i,j)}^0}{\Delta t} &= \lambda_b d_b \left(\frac{T_{b(i+1,j)}^1 - 2T_{b(i,j)}^1 + T_{b(i-1,j)}^1}{\Delta x^2} + \frac{T_{b(i,j+1)}^1 - 2T_{b(i,j)}^1 + T_{b(i,j-1)}^1}{\Delta y^2} \right) \\ &+ \frac{T_{pv(i,j)}^1 - T_{b(i,j)}^1}{R_{b,pv}} + \frac{T_a - T_{b(i,j)}^1}{R_{b,a}} \end{aligned} \tag{25}$$

For the connection nodes of the absorber plate:

$$\begin{aligned} \rho_b c_b d_b \frac{T_{b(i,11)}^1 - T_{b(i,11)}^0}{\Delta t} &= \lambda_b d_b \left(\frac{T_{b(i+1,11)}^1 - 2T_{b(i,11)}^1 + T_{b(i-1,11)}^1}{\Delta x^2} + 2\frac{T_{b(i,10)}^1 - T_{b(i,11)}^1}{\Delta y^2} \right) \\ &+ \frac{T_{pv(i,11)}^1 - T_{b(i,11)}^1}{R_{b,pv}} + \frac{T_{t(i-1,1)}^1 - T_{b(i,11)}^1}{R_{b,t} \cdot A_{ij}} \end{aligned} \tag{26}$$

For the copper tube:

$$\begin{aligned} A_t \rho_t c_t \frac{T_{t(i,1)}^1 - T_{t(i,1)}^0}{\Delta t} &= A_t \lambda_t \frac{T_{t(i+1,1)}^1 - 2T_{t(i,1)}^1 + T_{t(i-1,1)}^1}{\Delta x^2} \\ + \pi D_t h_{w,t} (T_{w(i,1)}^1 - T_{t(i,1)}^1) &+ \frac{T_{b(i+1,11)}^1 - T_{t(i,1)}^1}{R_{b,t} \cdot \Delta x} \end{aligned} \tag{27}$$

For the water in the copper tube:

$$\begin{aligned} A_w \rho_w c_w \frac{T_{w(i,1)}^1 - T_{w(i,1)}^0}{\Delta t} &= -\dot{m} c_w \frac{T_{w(i-2,1)}^1 - 4T_{w(i-1,1)}^1 + 3T_{w(i,1)}^1}{2\Delta x} \\ + A_w \lambda_w \frac{T_{w(i+1,1)}^1 - 2T_{w(i,1)}^1 + T_{w(i-1,1)}^1}{\Delta x^2} &+ P_w h_{w,t} \left(T_{t(i,1)}^1 - T_{w(i,1)}^1 \right) \end{aligned} \tag{28}$$

In these equations, the superscript “0” represents the results of the previous time and “1” refers to the results of the current time.

To predict the performance of the a-Si PV/T system, a numerical simulation program of the model written in MATLAB is developed. Fig. 7 shows the daily flow chart of the calculation process for the a-Si PV/T system. The weather data such as solar radiation, ambient temperature can be obtained from actual experimental data. The time step Δt for the model is 2 s. When the error between two iterations is less than the acceptable tolerance (10^{-5}), the system is considered to reach the steady-state and then moves to next time.

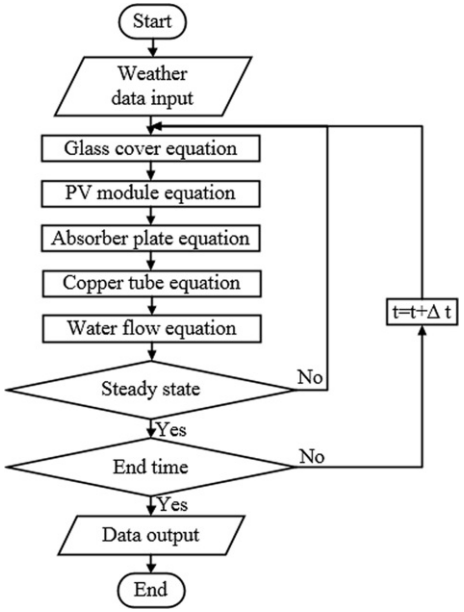

Fig. 7 Daily flow chart of the calculation process for the a-Si PV/T system.

5 Results and discussion

5.1 Experimental results at medium operating temperature

5.1.1 Long-term experimental results at the operating temperature of 60 °C

Experiments on the long-term behavior of the a-Si PV/T system at medium operating temperature have been carried out. There is no sign of technical failure by 31 March 2019. The results from December 2017 to November 2018 are summarized in this section. During the test period, the inlet water temperature with a fixed value of 60 °C was controlled by a thermostatic water tank. The test results for three typical days (January 9, 2018, June 6, 2018 and November 27, 2018) are summarized, which respectively represent the system performance at the initial, intermediate and final phases of the experiments. In these three days, the outdoor experiments lasted from 10:00 to 15:00. The actual measured ambient temperature and solar radiation are shown in Fig. 8. During the test, the daily average ambient temperatures were 5.3 °C, 26.3 °C and 21.0 °C; the total solar radiations each were 15.17 MJ/m^2, 16.35 MJ/m^2 and 12.64 MJ/m^2.

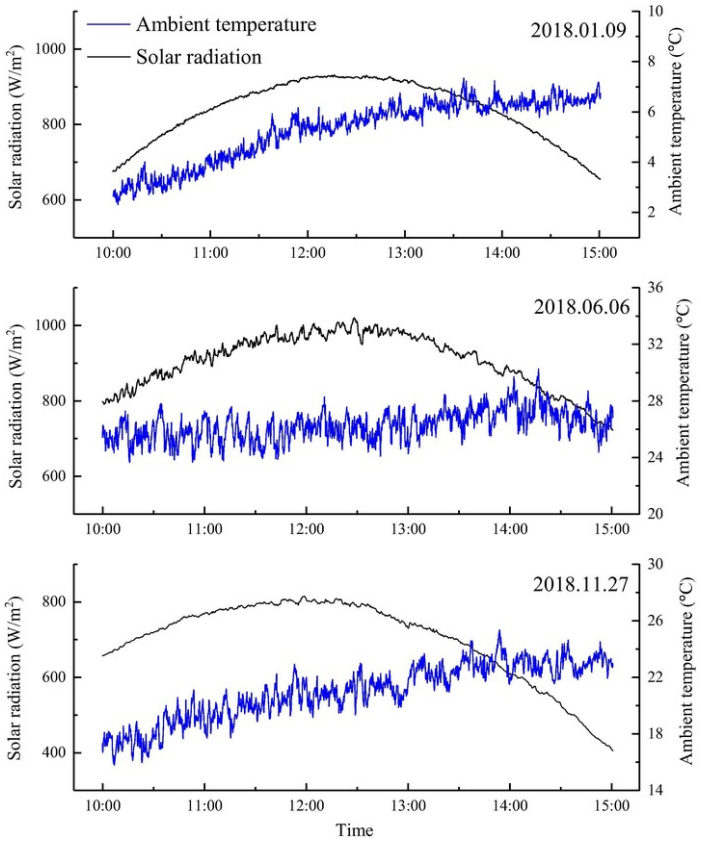

Fig. 8 Variations of ambient temperature and solar radiation.

The thermal and electrical performance of the a-Si PV/T system are shown in Figs. 9, 10 and 11. The trends of the thermal gain and electrical power of the system were highly correlated with the variation of solar radiation. The total heat gains on January 9, June 6, and November 27 were 1.31, 2.19 and 1.18 kWh, with an average thermal efficiency of 16.74%, 26.01% and 18.09%, respectively. The level of the thermal efficiency was related to the ambient temperature. The lower the ambient temperature, the larger the heat loss between the collector and surrounding ambient, resulting in lower thermal efficiency. At given solar radiation, less solar energy is converted into electricity by the a-Si cells due to the lower PV efficiency than that by c-Si cells and therefore more energy will be dissipated into heat and transferred to water, resulting in a higher thermal efficiency. However, the spectral absorptivities of the a-Si and c-Si cells are different. Since the commercial a-Si cells are mainly used for solo power purpose, the absorptivity of the a-Si cells is higher in the wavelength range of spectral response (between 0.35 μm and 0.75 μm), but is lower in other regions. It is found that the average absorptivity of the a-Si solar cells in solar irradiation spectrum is 0.76, which is lower than c-Si cells (about 0.9). Thus, less solar radiation is absorbed by the a-Si PV/T collector, which may have a negative effect on the thermal efficiency. Due to the trade-off between the absorptivity and electricity conversion efficiency, the thermal efficiency of the a-Si PV/T collector might be lower than that of common c-Si PV/T collectors at the same conditions of operating temperature and solar radiation.

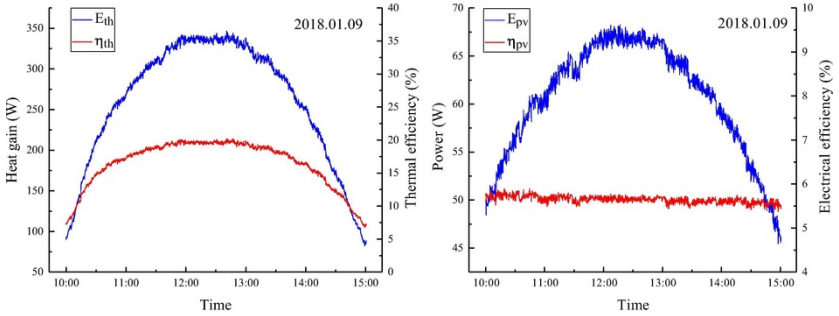

Fig. 9 Variations of thermal and electrical performance on January 9, 2018.

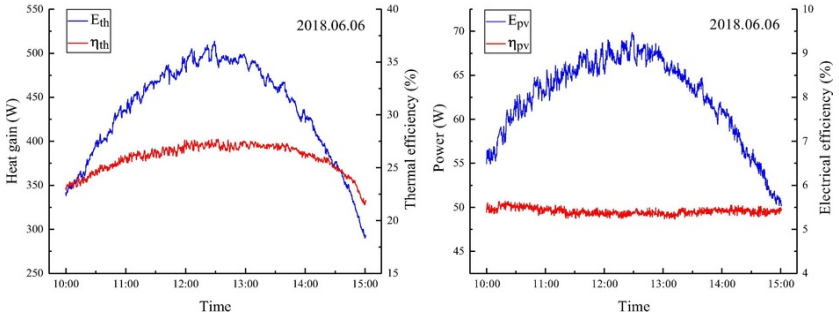

Fig. 10 Variations of thermal and electrical performance on June 6, 2018.

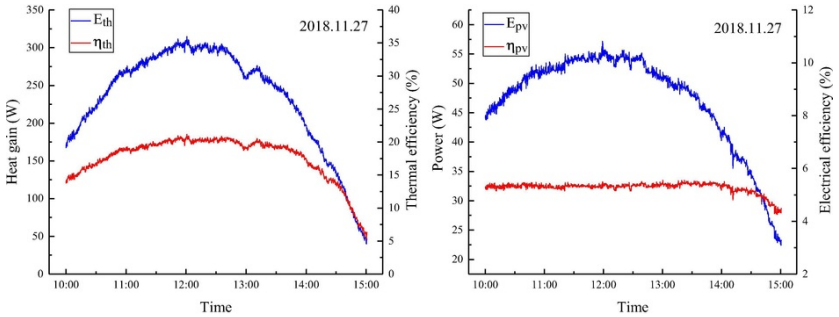

Fig. 11 Variations of thermal and electrical performance on November 27, 2018.

The total electrical powers were 0.30, 0.31 and 0.24 kWh at the initial, the intermediate and the final phases. The average electrical efficiencies were 5.65%, 5.41% and 5.30%, meanwhile the maximum electrical efficiencies were 5.73%, 5.64% and 5.55%. There was a significant drop in electrical efficiency due to the Staebler-Wronski (S-W) effect [51]. The S-W effect is related with the light-induced degradation of electrical performance and the creation of defect states.

Table 2 shows the multi-day experimental results at medium operating temperature from December 2017 to November 2018. The weathers for these 40 days were all sunny or cloudy. The experimental results including the total heat gain, average thermal efficiency, total electrical power and average electrical efficiency were calculated and organized. Fig. 12 presents the variations of the electrical efficiency during long-term experiments. Due to the light-induced degradation of electrical performance, the electrical efficiency presented a downward trend. The average electrical efficiency on December 25, 2017 was the highest at 5.69%, while the electrical efficiency was reduced to 5.22% through long-term operation for about one year. It is observed that the electrical efficiencies of the serial numbers 5–12 and 33–44 were significantly lower than the linear fitting curve, while the values of the numbers 13–32 were mostly over the linear fitting curve. This phenomenon was related to the seasonal variation of a-Si cells. Due to the S-W effect and spectral effect, a-Si cells exhibited higher electrical efficiency in summer but lower electrical efficiency in winter, which was different from c-Si cells [52,53].

Table 2 Multi-day experimental results of a-Si PV/T system at medium operating temperature.

Number	Date	$\overline{T_a}$ (∘C)	$\dot{m}$ (kg/s)	H (MJ/m²)	Q_{th} (kWh)	$\eta_{th,a}$ (%)	Q_{pv} (kWh)	$\eta_{pv,a}$ (%)
1	12.25	10.2	0.036	12.80	1.09	16.47	0.26	5.69
2	12.26	12.5	0.036	11.37	0.90	15.38	0.22	5.62
3	1.09	5.3	0.036	15.17	1.31	16.74	0.30	5.65
4	1.10	4.1	0.044	14.49	1.27	17.08	0.29	5.64
5	1.11	3.9	0.028	13.92	1.05	14.69	0.27	5.57
6	1.12	2.6	0.036	14.48	1.12	15.08	0.28	5.52
7	3.09	11.9	0.028	15.41	1.60	20.15	0.30	5.47
8	3.10	16.7	0.026	16.60	1.85	21.63	0.32	5.41
9	3.11	19.3	0.028	16.56	1.97	23.12	0.32	5.44
10	3.12	22.0	0.026	16.17	2.16	25.93	0.31	5.46
11	3.13	23.6	0.042	15.79	2.50	30.77	0.31	5.50
12	3.23	19.7	0.042	16.23	2.54	30.36	0.31	5.40
13	3.26	22.6	0.043	14.27	2.29	31.16	0.28	5.52
14	3.27	22.88	0.031	15.08	2.21	28.45	0.30	5.54
15	3.31	26.0	0.031	14.67	2.25	29.85	0.29	5.62
16	4.02	28.5	0.031	14.09	2.14	29.54	0.28	5.63
17	4.09	24.2	0.039	16.91	2.63	30.25	0.33	5.45
18	4.17	21.9	0.031	16.14	2.43	29.26	0.31	5.44
19	4.18	25.2	0.033	16.56	2.59	30.40	0.32	5.45
20	5.09	25.0	0.031	16.36	2.39	28.42	0.32	5.46
21	5.10	23.0	0.028	13.31	1.43	20.89	0.26	5.44
22	6.06	26.3	0.026	16.35	2.19	26.01	0.31	5.41
23	6.07	34.1	0.028	13.76	2.00	28.20	0.27	5.55
24	6.11	35.0	0.026	14.91	2.24	29.15	0.29	5.46
25	6.12	36.9	0.023	15.19	2.12	27.13	0.29	5.47
26	6.13	35.0	0.023	14.94	2.09	27.17	0.29	5.48
27	6.15	35.8	0.023	13.77	1.82	25.69	0.27	5.53
28	10.29	24.9	0.031	15.41	1.98	25.02	0.29	5.40
29	10.30	23.2	0.031	12.34	1.41	22.19	0.24	5.39
30	10.31	21.7	0.031	13.20	1.46	21.53	0.25	5.39
31	11.01	20.1	0.028	14.46	1.43	19.22	0.28	5.43
32	11.02	19.2	0.034	14.64	1.38	18.34	0.28	5.48
33	11.22	15.2	0.029	13.39	1.15	16.67	0.25	5.27

34	11.23	14.8	0.026	13.72	0.99	14.04	0.26	5.31
35	11.24	18.0	0.028	12.17	1.04	16.58	0.23	5.29
36	11.25	17.7	0.026	11.13	0.78	13.61	0.21	5.21
37	11.26	17.17	0.029	12.27	1.07	16.94	0.23	5.20
38	11.27	21.0	0.029	12.64	1.18	18.09	0.24	5.30
39	11.28	18.8	0.029	11.79	0.96	15.77	0.22	5.33
40	11.29	19.4	0.029	9.53	0.59	11.96	0.18	5.22

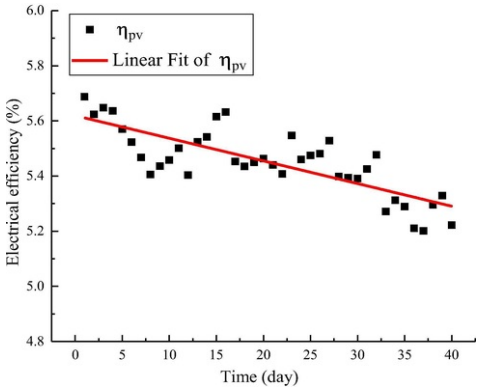

Fig. 12 Variations of the electrical efficiencies during long-term experiments.

Notably, the system was shut down and cooled down at night. The PV/T module thereby operated in recurrent alternating heating and cooling conditions. During day time, the PV/T was running at medium temperature, while could be at significantly low temperature at night. No interruption or observable deformation appeared in the a-Si PV/T collector during the long-term tests, thus the technical feasibility of the a-Si PV/T system at medium operating temperature can be demonstrated preliminarily.

5.1.2 Experimental results at the operating temperature of 70 °C

To investigate the performance of the a-Si PV/T system at higher operating temperature, the experiment was conducted from 10:00 to 15:00 on March 7, 2019 with the fixed inlet temperature of 70 °C and mass flow rate of about 0.044 kg/s. As shown in Fig. 13, the ambient temperature ranged from 7.8 °C to 14.6 °C, with the daily average ambient temperature of 11.6 °C. The total solar radiation received by the collector could reach 16.46 MJ/m^2. Fig. 14 shows the thermal and electrical performance of the a-Si PV/T system at the operating temperature of 70 °C. The total heat gain and electrical power were 1.88 kWh and 0.30 kWh, meanwhile the corresponding thermal efficiency and electrical efficiency were 22.02% and 5.10%, respectively.

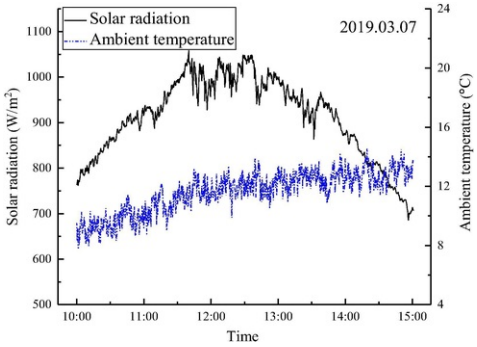

Fig. 13 Variations of ambient temperature and solar radiation on March 7, 2019.

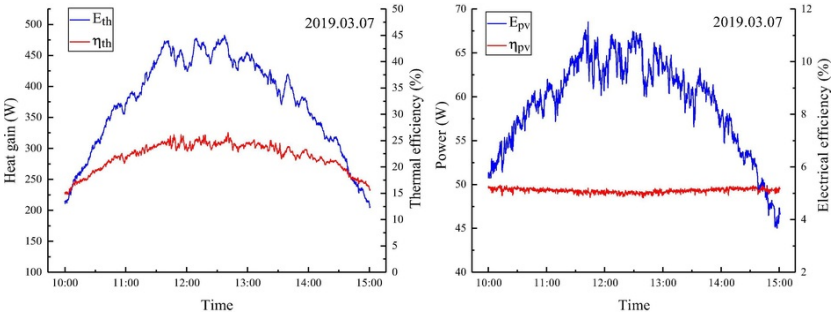

Fig. 14 Variations of thermal and electrical performance on March 7, 2019.

5.1.3 Experimental results at the operating temperature of 80 °C

The outdoor experiment at the operating temperature of 80 °C was also carried out on March 10, 2019. The mass flow rate was similar to that of March 7, about 0.042 kg/s. As shown in Fig. 15, the average ambient temperature was nearly 16.5 °C (ranged from 12.9 °C to 19.8 °C), and the total solar radiation was 13.96 MJ/m^2. There was a significant drop in solar radiation between 12:00 and 13:00, which caused a decline in heat gain and electrical power, as shown in Fig. 16. The total heat gain and average thermal efficiency were 1.02 kWh and 13.87% during the test time. Increase in the operating temperature enhanced the heat loss between the PV/T collector and surrounding air, thereby the thermal efficiency was lower than that on March, 7. Besides, the total electrical power and average electrical efficiency were 0.24 kWh and 4.81%.

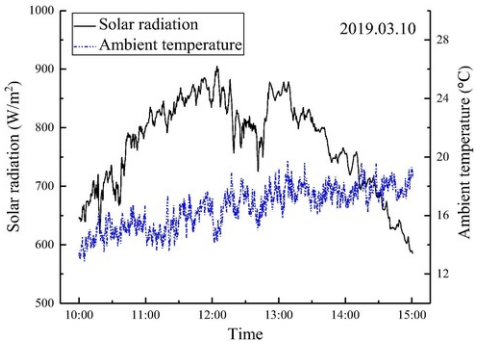

Fig. 15 Variations of ambient temperature and solar radiation on March 10, 2019.

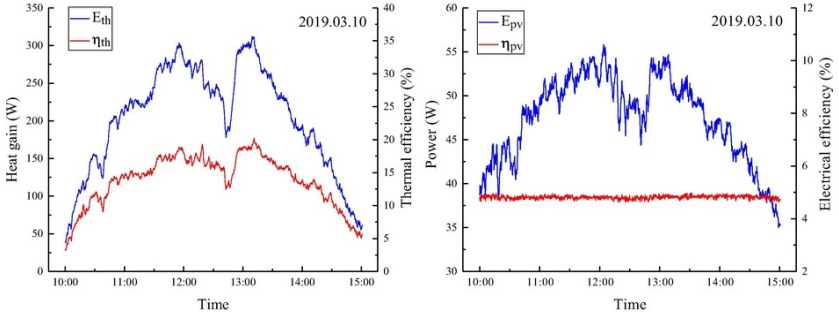

Fig. 16 Variations of thermal and electrical performance on March 10, 2019.

5.1.4 Regression formulation of thermal efficiency

According to the experimental results on March 7 and March 10 with the same water flow rate, the relationship between thermal efficiency and $(T_{in} - T_a)/G$ is given in Fig. 17. The thermal efficiency can be expressed by the regression formula:

$$\eta_{th} = 0.4936 - 4.241\frac{T_{in} - T_a}{G} \tag{29}$$

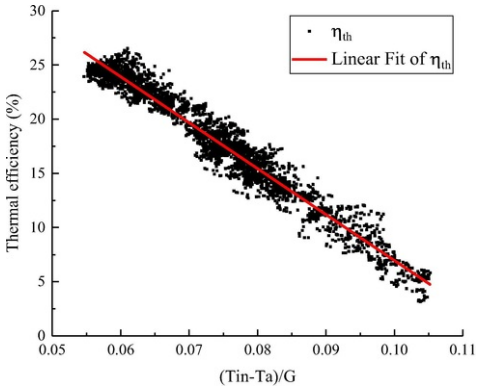

Fig. 17 Plot of thermal efficiency of a-Si PV/T collector.

As presented in the regression line, the intercept thermal efficiency is 49.36%. With the increase of $(T_{in} - T_a)/G$, the thermal efficiency decreased gradually with a slope of −4.241.

5.1.5 Uncertainly analysis of experiment

The uncertainties of the measurements need to be analyzed due to the possible measurement errors of measuring instruments. The calculation of uncertainty is given by

$$\Delta y = \left[\left(\frac{\partial f}{\partial x_1}\right)^2 (\Delta x_1)^2 + \left(\frac{\partial f}{\partial x_2}\right)^2 (\Delta x_2)^2 + \cdots + \left(\frac{\partial f}{\partial x_n}\right)^2 (\Delta x_n)^2\right]^{\frac{1}{2}} \tag{30}$$

where f is the function of indirect measurement that requires an uncertainty analysis; x is one of the variables of the function; Δx is the absolute error of the variable.

When the operating temperature were 60 °C, 70 °C and 80 °C on November 27, 2018, March 7, 2019 and March 10, 2019, the average uncertainties of the thermal efficiency during the test time each were ±1.65%, ±1.94%, ±1.92%; the uncertainties of the electrical efficiency were ±0.11%, ±0.10% and ± 0.10%. Therefore, the measuring instruments could ensure good accuracy of the experimental results.

5.2 Numerical analysis

Some temperature sensors have been placed in the PV/T system, which can measure the temperatures of the aluminum absorber plate, water inlet and outlet. However, it is difficult to measure the temperature of the PV cells

which are well encapsulated and laminated. The distributed parameter model is used to investigate the temperature profile of the PV/T module, and thereby an inside view of heat transfer and power conversion can be provided. The model is validated by experimental tests.

5.2.1 Inside views of temperature distribution

As shown in the Fig. 18, the area of a single copper tube and half absorber plate on each side of the copper tube are displayed (inside the blue lines). The temperature distributions of the PV module and absorber plate are presented in Figs. 19 and 20. The boundary conditions in the simulation are set up based on the test conditions at noon. The solar radiation, wind velocity, water mass flow rate and ambient temperature are about 1000 W/m^2, 2 m/s, 0.04 kg/s and 30 °C. It is observed that the temperatures of the PV module and absorber plate gradually increase along the direction of the water flow of the x-axis. The temperatures of the intermediate absorber plate and PV module (connected with the copper tube) are lower than that on the both sides. When the inlet water temperatures are 60 °C, 70 °C, and 80 °C, the average temperatures of the absorber plate are 70.8 °C, 79.0 °C, 85.5 °C; the average temperatures of the PV module are 71.8 °C, 79.9 °C, and 86.1 °C. In addition, the temperature distributions of the PV module are more uniform than that of the absorber plate. The temperature differences between the maximum and minimum temperature of the PV module are 4.0 °C, 3.3 °C and 2.0 °C at the inlet water temperatures of 60 °C, 70 °C and 80 °C, and the temperature differences of the absorber plate are 5.8 °C, 4.8 °C and 2.9 °C. As the operating temperature increases, the temperature differences of the PV module and absorber plate gradually decrease and the temperature distributions become more uniform.

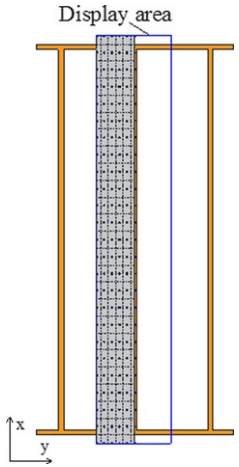

Fig.18 Display area of the PV module and absorber plate.

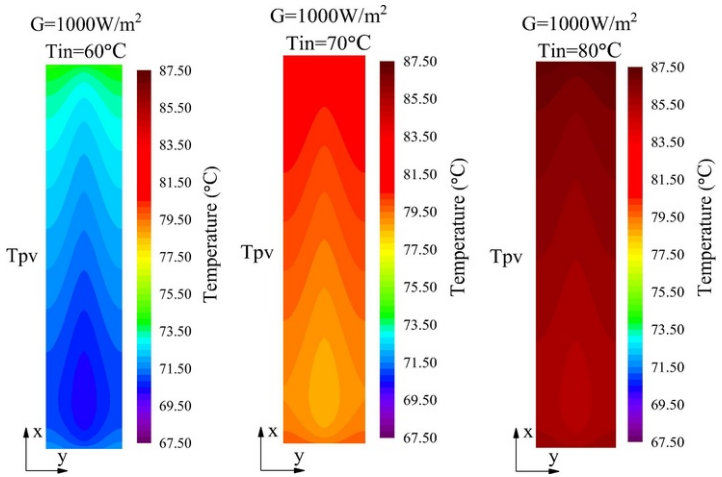

Fig. 19 Temperature distributions of the PV module at different inlet temperatures.

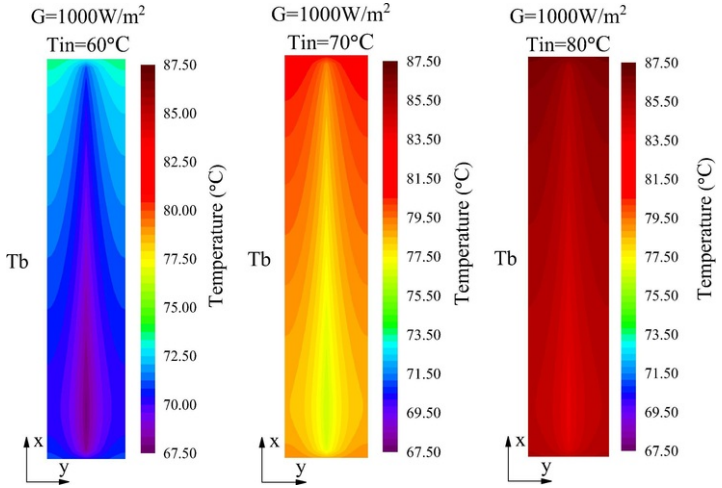

Fig. 20 Temperature distributions of the absorber plate at different inlet temperatures.

The temperature distributions of the PV module and the absorber plate at different solar radiations are also investigated. As shown in the Figs. 21 and 22, with the solar radiation increasing from 400 W/m^2 to 1000 W/m^2, the average temperature of the PV module is enhanced from 61.4 °C to 71.8 °C and the average temperature of the absorber plate increases from 61.2 °C to 70.8 °C. Although the inlet water temperature is set to 60 °C, the temperature of PV module can exceed 70 °C at high levels of solar radiation, even as high as 74.3 °C. The feasibility of the a-Si PV/T system at medium operating temperature can be further demonstrated.

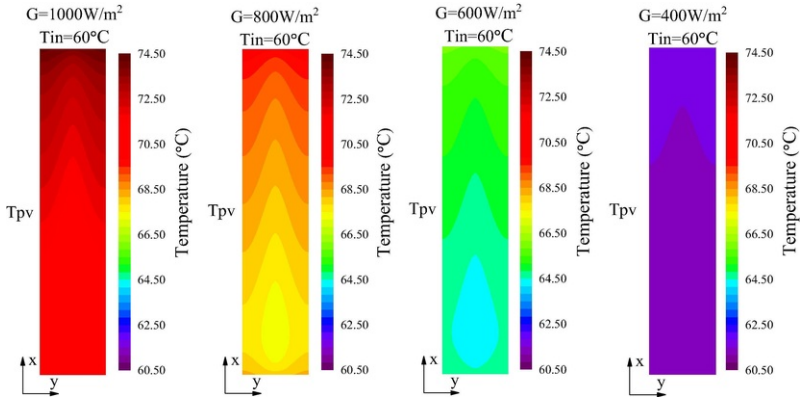

Fig. 21 Temperature distributions of the PV module at different solar radiations.

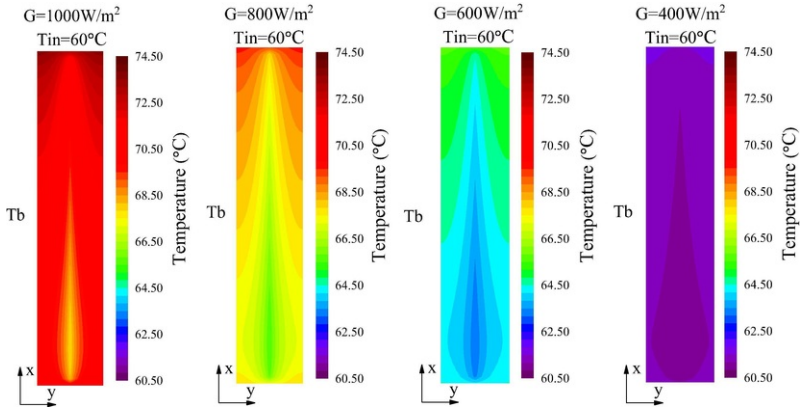

Fig. 22 Temperature distributions of the absorber plate at different solar radiations.

5.2.2 Experimental validation

To validate the accuracy of the mathematical model of the a-Si PV/T system, the actual environment parameters such as the ambient temperature, solar radiation, inlet water temperature and water flow rate were employed in the numerical simulation study. Figs. 23 and 24 show a series of experimental and simulation results of the a-Si PV/T system at the operating temperature of 60 °C on November 27, 2018. It can be observed from these figures that the simulation and experimental results are follow a same trend with minor difference. The average thermal efficiency is 18.09% experimentally and 18.49% numerically, and the average electrical efficiency is 5.30% for experiment and 5.36% for simulation. For the absorber plate temperature, outlet water temperature, thermal efficiency, and electrical efficiency, the MREs each are 0.15%, 0.08%, 3.27%, and 2.20%. The proximity in magnitude and similarity in trend between the experimental and simulation results validate the mathematical model of the a-Si PV/T system.

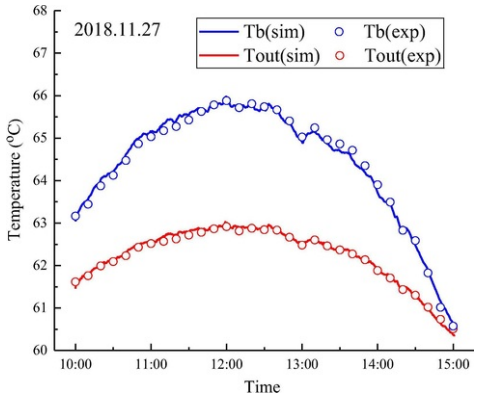

Fig. 23 Experimental and simulation results of absorber plate and outlet temperature at the operating temperature of 60 °C.

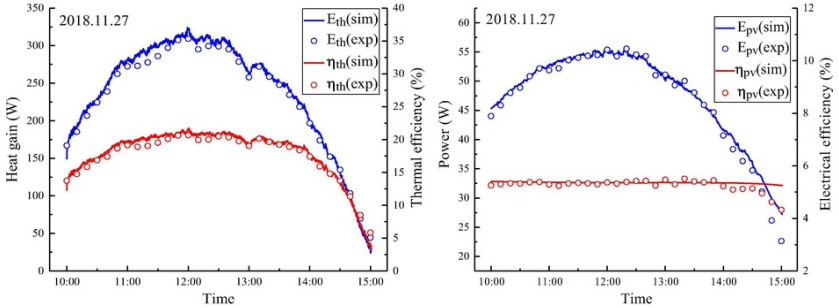

Fig. 24 Experimental and simulation results of thermal and electrical performance at the operating temperature of 60 °C.

Similarly, comparisons between the simulation and experimental results of the a-Si PV/T system at the operating temperature of 40, 70 and 80 °C are carried out. 40 °C represents the PV/T operating temperature in heating season. The error analysis of the experimental and simulation results is shown in Table 3. The MRE of the thermal efficiency has the maximum value among the four parameters of about 5.83%. The MRE of electrical efficiency is between 1.10% and 2.78%, and for the absorber plate temperature and outlet temperature, the maximum value is only 1.10%. Therefore, the close concordance of the simulation results of the thermal and electrical efficiency with those of the experimental at different medium operating temperatures confirms the effectiveness of the proposed mathematic model.

Table 3 MREs between the simulation and the experimental results at different operating temperatures.

T_{in} (°C)	MRE (%)			
	η_{th}	η_{pv}	T_b	T_{out}
40	5.83	2.78	1.10	0.34
60	3.27	2.20	0.15	0.08
70	2.54	1.10	0.31	0.11
80	4.99	1.96	0.21	0.07

5.2.3 Grid independence test

The grid independence test is conducted to examine the accuracy of the model and the control volume changes from 153 to 1020. The simulation is carried out under the following fixed values: wind velocity of 2 m/s, mass flow rate of 0.04 kg/s, inlet temperature of 60 °C, solar radiation of 800 W/m^2, and ambient temperature of 20 °C. As shown in Fig. 25, the results reveal that the variations of the thermal and electrical efficiency are not sensitive to the number of control volumes, especially when the control volume is more than 400. As the control volume increases from 153 to 1020, the thermal efficiency changes from 25.60% to 24.36%, and the electrical efficiency varies from 5.35% to 5.36%. Considering that the program executing time will be significantly prolonged with increasing control volumes, 561 control volumes are applied in this study.

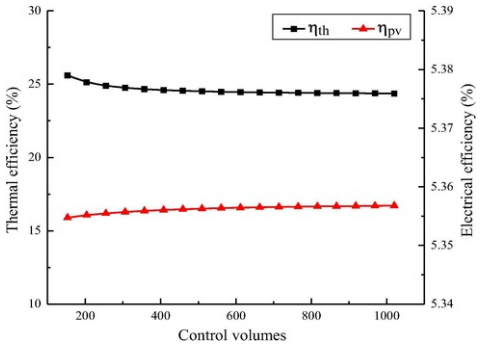

Fig. 25 Variation of the thermal and electrical efficiency as the change of control volumes.

5.3 Performance prediction

The a-Si PV/T system is promising because medium-grade heat can be provided for solar cooling, thermoelectric generation and ORC in summer and low-grade heat can be used for space heating in winter. Take Hefei for example, the non-heating season is generally from April to October, and the other months are the heating season according to the local climate. In non-heating season, the a-Si PV/T system runs at medium temperature (e.g. 60 °C, 70 °C and 80 °C). In heating season, the operating temperature is 40 °C, and the hot water can be used for heating homes and offices.

5.3.1 Performance in the non-heating season

To evaluate the performance of the a-Si PV/T system at medium operating temperature in non-heating season, a typical weather data in non-heating season is selected. The hourly weather data in Hefei are obtained from the EnergyPlus [54] and are shown in Fig. 26. The ambient temperature increases from 32.1 °C to 34.9 °C, and the hourly solar radiation ranges from 754.80 W/m^2 to 933.93 W/m^2. Based on the validated mathematical model, the performance of the a-Si PV/T system at different medium operating temperatures (such as 60 °C, 70 °C, and 80 °C) can be further investigated. The simulations also commence at 10:00 and end at 15:00. Fig. 27 shows the thermal and electrical performance of the a-Si PV/T system at different operating temperatures. The values of the thermal and electrical efficiency are marked on the top of column chart. With the increasing operating temperature, the heat gain and electrical power are reduced. For instance, with the temperature of 60 °C, 70 °C and 80 °C, the hourly heat gains between 12:00 and 13:00 are 584.50 W, 465.87 W and 343.42 W; the electrical powers are 62.68 W, 60.27 W and 57.87 W, respectively.

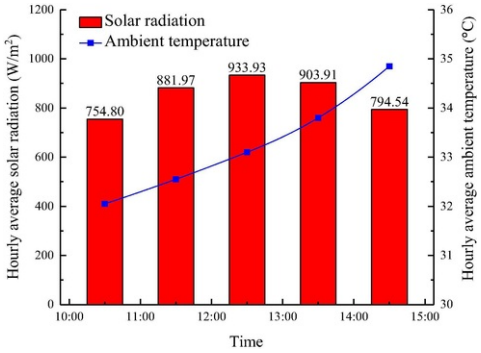

Fig. 26 Hourly solar radiation and ambient temperature.

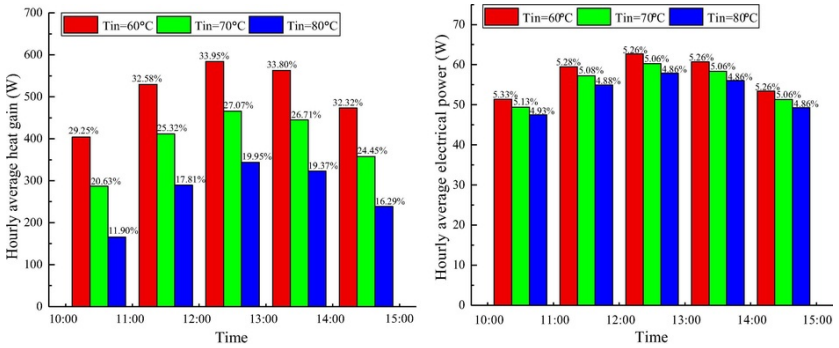

Fig. 27 Hourly thermal and electrical performance of the a-Si PV/T system at different operating temperatures.

Table 4 presents the daily performance of the a-Si PV/T system at different operating temperatures in non-heating season. As the operating temperature increased from 60 °C to 80 °C, there is 15.10% decrease in daily average thermal efficiency, but only 0.4% decrease in the electrical efficiency.

Table 4 Daily performance of the a-Si PV/T system at different operating temperatures.

T_{in} (°C)	$\overline{T_a}$ (∘C)	H (MJ/m²)	Q_{th} (kWh)	$\eta_{th,a}$ (%)	Q_{pv} (kWh)	$\eta_{pv,a}$ (%)
60	33.3	15.37	2.55	32.29%	0.29	5.28
70			1.97	24.87%	0.28	5.08
80			1.36	17.19%	0.27	4.88

5.3.2 Annual performance

The annual performance of the a-Si PV/T system is analyzed by the simulation according to the meteorological data of a typical meteorological year in Hefei. The daily operation time of the a-Si PV/T system is from 10:00 am to 15:00 pm. The monthly average solar radiation and ambient temperature obtained from the EnergyPlus are shown in Fig. 28 [54]. Fig. 29 shows the monthly heat gain and electrical power of the a-Si PV/T system. The blue column chart indicates the results in heating season with the inlet water temperature of 40 °C, and the red one represents the values in non-heating season with the temperature of 60 °C. The maximum monthly heat gain and electrical power occur in August with the value of 1.18 kWh/day and 0.18 kWh/day, and the minimum values are about 0.42 kWh/day and 0.11 kWh/day in January, respectively. As shown in Fig. 30, the monthly heat gain and electrical power of the a-Si PV/T system working at different operating temperatures are calculated and compared in non-heating season. As the operating temperature increases, the thermal gain decreases significantly due to the large heat loss, while the electrical power only decreases slightly. The annual performance of the a-Si PV/T system displayed in Table 5 is calculated according to the results shown in Figs. 29 and 30.

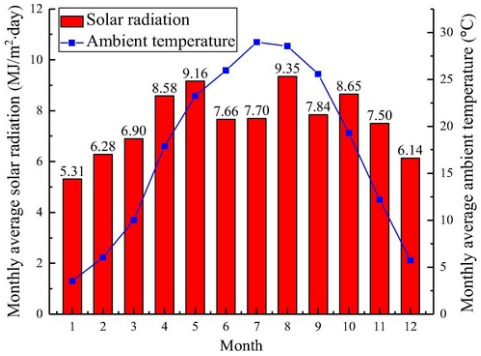

Fig. 28 Monthly average solar radiation and ambient temperature.

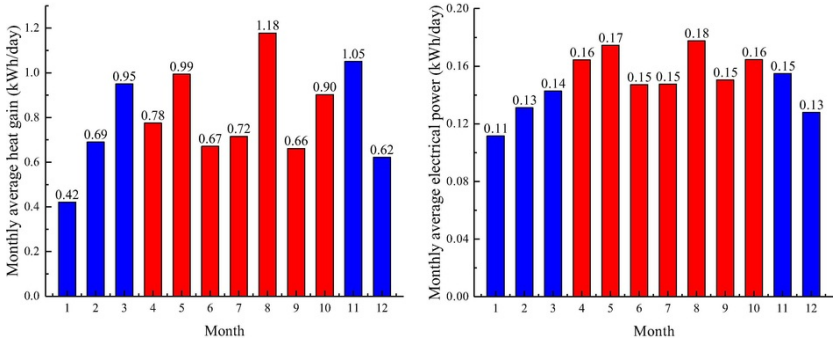

Fig. 29 Monthly heat gain and electrical power of the a-Si PV/T system.

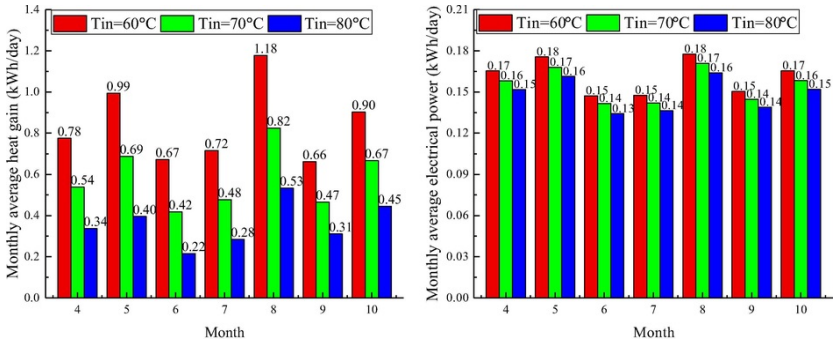

Fig. 30 Monthly heat gain and electrical power in non-heating season at different operating temperatures.

Table 5 Annual performance of the a-Si PV/T system.

	Temperature (°C)	H (MJ/m²)	Q_w (kWh)	E_{pv} (kWh)
Heating season	40	969.79	112.62	20.17
Non-heating season	60	1802.98	180.75	34.45
	70		124.96	33.14
	80		49.53	31.83

Since the above studies are based on the conventional flat collector, the thermal efficiency is not high enough at medium operating temperature. Fortunately, based on the experimental and simulation studies, the feasibility of the a-Si PV/T system for medium temperature application can be demonstrated. On this foundation, we can apply a-Si cells in vacuum PV/T system and compound parabolic concentrator PV/T system to meet the demand for higher thermal efficiency [55,56].

6 Conclusion

In this study, a novel a-Si PV/T system has been designed and constructed to investigate the performance at medium temperature. A distributed parameter model is established and validated by outdoor experiments. The results are summarized as follows.

(1) Experiments on the long-term behavior of the a-Si PV/T system at medium operating temperature (60 °C) were carried out from December 2017 to November 2018. At the initial, intermediate and final phases of the long-term tests, the average thermal efficiencies were 16.75%, 26.01% and 18.09%; the average electrical efficiencies were 5.65%, 5.41%, and 5.30%, respectively. After the long-term operation at medium temperature, no interruption or observable deformation has taken place in the a-Si PV/T system.

(2) The outdoor experiments were also conducted at the operating temperature of 70 °C and 80 °C with the thermal efficiency of 22.02% and 13.87%. The electrical efficiencies at the operating temperature of 70 °C and 80 °C were 5.10% and 4.81%.

(3) The simulation results of the a-Si PV/T system at the operating temperature of 40 °C, 60 °C, 70 °C and 80 °C are compared with experimental data. The MREs of the thermal efficiency and electrical efficiency are below 5.83% and 2.78%, which can prove the effectiveness of the mathematical model in predicting the performance of the a-Si PV/T system.

(4) In non-heating season, a typical day is selected to investigate the performance of the a-Si PV/T system at different medium operating temperatures. The thermal efficiencies at the operating temperatures of 60 °C, 70 °C and 80 °C are 32.29%, 24.87% and 17.19%; the electrical efficiency are 5.28%, 5.08% and 4.88%, respectively.

(5) The annual performance of the a-Si PV/T system is analyzed covering the non-heating season (April to October) and heating season (November to March). In heating season, the operating temperature is 40 °C, and the thermal gain and the electrical power are 112.62 kWh and 20.17 kWh. In non-heating season, the thermal gain and the electrical power are 180.75 kWh and 34.45 kWh with the operating temperature of 60 °C.

(6) Based on the experimental and simulated results, the technical and thermodynamic feasibility of the a-Si PV/T system for medium temperature application is demonstrated.

Acknowledgments

This study was sponsored by EU Marie Curie International Incoming Fellowships Program (703746), National Key R&D Plan (2016YFE0124800), the National Science Foundation of China (NSFC 51776193, and 51761145109), and Bureau of International Cooperation, Chinese Academy of Sciences (211134KYSB20160005).

References

[1] T.T. Chow, A review on photovoltaic/thermal hybrid solar technology, *Appl Energy* **87**, 2010, 365–379.

[2] Mohammad Alobaid, Ben Hughes, John Kaiser Calautit, Dominic O'Connor and Andrew Heyes, A review of solar driven absorption cooling with photovoltaic thermal systems, *Renew Sustain Energy Rev* **76**, 2017, 728–742.

[3] Wei He, Gan Zhang, Xingxing Zhang, Jie Ji, Guiqiang Li and Xudong Zhao, Recent development and application of thermoelectric generator and cooler, *Appl Energy* **143** (1), 2015, 1–25.

[4] Kiyarash Rahbar, Alireza Riasi, Hamed Khatam Bolouri Sangjoeei and Nima Razmjoo, Heat recovery of nano-fluid based concentrating Photovoltaic Thermal (CPV/T) Collector with Organic Rankine Cycle, *Energy Convers Manag* **179** (1), 2019, 373–399.

[5] G. Vokas, N. Christandonis and F. Skittides, Hybrid photovoltaic–thermal systems for domestic heating and cooling—a theoretical approach, *Sol Energy* **80** (5), 2006, 607–615.

[6] G. Mittelman, A. Kribus and A. Dayan, Solar cooling with concentrating photovoltaic/thermal (CPVT) systems, *Energy Convers Manag* **48** (9), 2007, 2481–2490.

[7] I. Elsafty and A.J. Al-Daini, Economic comparison between a solar powered vapor absorption air conditioning system and a vapor compression system in the Middle East, *Renew Energy* **25**, 2002, 569–583.

[8] E.A. Chávez-Urbiola, Yu.V. Vorobiev and L.P. Bulat, Solar hybrid systems with thermoelectric generators, *Sol Energy* **86**, 2012, 369–378.

[9] A. Rezania and L.A. Rosendahl, Feasibility and parametric evaluation of hybrid concentrated photovoltaic-thermoelectric system, *Appl Energy* **187**, 2017, 380–389.

[10] Jing Li, Gang Pei, Yunzhu Li and Jie Ji, Novel design and simulation of a hybrid solar electricity system with organic Rankine cycle and PV cells, *Int. J. Low-Carbon Tech.* **4** (5), 2010, 223–230.

[11] Andrea De Pascale, Claudio Ferrari, Francesco Melino, Mirko Morini and Michele Pinelli, Integration between a thermophotovoltaic generator and an Organic Rankine Cycle, *Appl Energy* **97**, 2012, 695–703.

[12] Konstantin Tourkov and Laura Schaefer, Performance evaluation of a PVT/ORC (photovoltaic thermal/organic Rankine cycle) system with optimization of the ORC and evaluation of several PV (photovoltaic) materials, *Energy* **82**, 2015, 839–849.

[13] Gupchang Zhao, Liping Song, Xiaochen Hou and Yong Wang, Thermodynamic optimization of the organic Rankine cycle in a concentrating photovoltaic/thermal power generation system, *Appl Mech Mater* **448**, 2014, 1514–1518.

[14] Can Coskun, Ugurtan Toygar, Ozgur Sarpdag and Zuhal Oktay, Sensitivity analysis of implicit correlations for photovoltaic module temperature: a review, *J Clean Prod* **164**, 2017, 1474–1485.

[15] E. Radziemska, The effect of temperature on the power drop in crystalline silicon solar cells, *Renew Energy* **28**, 2003, 1–12.

[16] W.C. O'Mara, R.B. Herring and I.P. Hunt, Handbook of semiconductor silicon technology, 1990, Noyes Publications; Park Ridge, New Jersey, ISBN 0-8155-1237-6.

[17] Wim G.J. van Helden, Ronald J.Ch. van Zolingen and Herbert A. Zondag, PV thermal systems: PV panels supplying renewable electricity and heat, *Prog Photovolt: Res Appl* **12**, 2004, 415–426.

[18] Jean Zaraket, Michel Aillerie and Chafic Salame, Capacitance evolution of PV solar modules under thermal stress, *Energy Proc* **119**, 2017, 702–708.

[19] M. Shihabudheen and P. Arun, Performance evaluation of a hybrid photovoltaic-thermal water heating system, *Int J Green Energy* **11**, 2014, 969–986.

[20] Ji Jie, Pei Gang, He Wei, Sun Wei, Li Guiqiang, Li Jing. Research progress on solar photovoltaic/thermal systems utilization. Science Press, Beijing; 2017.08. ISBN: 9787030539793.

[21] M. Köntges, I. Kunze, S. Kajari-Schröder, X. Breitenmoser and B. Bjørneklett, The risk of power loss in crystalline silicon based photovoltaic modules due to micro-cracks, *Sol Energy Mater Sol Cells* **95**, 2011, 1131–1137

[22] M. Wang, J. Peng, N. Li, L. Lu and H. Yang, Experimental study on thermal performance of semi-transparent PV window in winter in Hong Kong, *Energy Proc* **105**, 2017, 864–868.

[23] Jinqing Peng, Lin Lu and Hongxing Yang, An experimental study of the thermal performance of a novel photovoltaic double-skin facade in Hong Kong, *Sol Energy* **97**, 2013, 293–304.

[24] Jinqing Peng, Lin Lu, Hongxing Yang and Tao Ma, Comparative study of the thermal and power performances of a semi-transparent photovoltaic façade under different ventilation modes, *Appl Energy* **138**, 2015, 572–583.

[25] Rustu Eke and Ali Senturk, Monitoring the performance of single and triple junction amorphous silicon modules in two building integrated photovoltaic (BIPV) installations, *Appl Energy* **109**, 2013, 154–162.

[26] W. Zhang, B. Hao and N. Li, Experiment and simulation study on the amorphous silicon photovoltaic walls, *Int J Photoenergy* **2014**, 2014, 643637.

[27] Ershuai Yin, Qiang Li and Yimin Xuan, Thermal resistance analysis and optimization of photovoltaic thermoelectric hybrid system, *Energy Convers Manage* **143**, 2017, 188–202.

[28] R. Bjørk and K.K. Nielsen, The performance of a combined solar photovoltaic (PV) and thermoelectric generator (TEG) system, *Sol Energy* **120**, 2015, 187–194.

[29] Platz R, Fischer D, Zufferey MA, Selvan JAA, Haller A, Shah A. Hybrid collectors using thin-film technology. In: Proceedings of 26th IEEE photovoltaic specialists conference; 1997. p. 1293–6.

[30] Tetsuyuki Ishii, Kenji Otani, Takashima and Shinji Kawai, Estimation of the maximum power temperature coefficients of PV modules at different time scales, *Sol Energy Mater Sol Cells* **95**, 2011, 386–389.

[31] G. Makrides, B. Zinsser, A. Phinikarides, M. Schubert and G.E. Georghiou, Temperature and thermal annealing effects on different photovoltaic technologies, *Renew Energy* **43**, 2012, 407–417.

[32] Ruther R, Tamizh-Mani G, del Cueto J, Adelstein J, Dacoregio MM, von Roedern B. Performance test of amorphous silicon modules in different climates-year three: higher minimum operating temperatures lead to higher performance levels. In: Proceedings of 31th IEEE photovoltaic specialists conference; 2005. p. 1635–8.

[33] M.J.M. Pathak, J.M. Peace and S.J. Harrison, Effect on amorphous silicon photovoltaic performance from high-temperature pulse in photovoltaic thermal hybrid devices, *Sol Energy Mater Sol Cells* **100**, 2012, 199–203.

[34] J.A. del Cueto and B. von Roedern, Temperature-induced changes in the performance of amorphous silicon multi-junction modules in controlled light-soaking, *Prog Photovolt Res Appl* **7**, 1999, 101–112.

[35] J. Yang, A. Banerjee and S. Guha, Triple-junction amorphous silicon alloy solar cell with 14.6% initial and 13.0% stable conversion efficiencies, *Appl Phys Lett* **70**, 1997, 2975–2977.

[36] E.L. Miller, R.E. Rocheleau and X.M. Deng, Design considerations for a hybrid amorphous silicon/photoelectrochemical multijunction cell for hydrogen production, *Int J Hydrogen Energy* **28**, 2003, 615–623.

[37] Benagli S, Borrello D, Vallat-Sauvain E, Meier J, Kroll U, Hoetzel J, et al. High-efficiency amorphous silicon devices on LPCVD-ZNO TCO prepared in industrial KAI-M R & D reactor. In: 24th European photovoltaic solar energy conference, Hamburg; September 2009.

[38] M.J.M. Pathak, K. Girotra, S.J. Harrison and J.M. Peace, The effect of hybrid photovoltaic thermal device operating conditions on intrinsic layer thickness optimization of hydrogenated amorphous silicon solar cells, *So Energy* **86**, 2012, 2673–2677.

[39] J. Rozario and J.M. Pearce, Optimization of annealing cycles for electric output in outdoor conditions for amorphous silicon photovoltaic–thermal systems, *Appl Energy* **148**, 2015, 134–414.

[40] S.A. Kalogirou and Y. Tripanagnostopoulos, Hybrid PV/T solar systems for domestic hot water and electrical production, *Energy Convers Manage* **47**, 2006, 3368–3382.

[41] Kanchan Vats and G.N. Tiwari, Energy and exergy analysis of a building integrated semitransparent photovoltaic thermal (BISPVT) system, *Appl Energy* **96**, 2012, 409–416.

[42] D. Ronak, I. Adnan, L.J. Goh, M.H. Ruslan and S. Kamaruzzaman, Predicting the performance of amorphous and crystalline silicon based photovoltaic solar thermal collectors, *Energy Convers Manage* **52**, 2011, 1741–1747.

[43] T. Nualboonrueng, P. Tuenpusa, Y. Ueda and A. Akisawa, Field experiments of PV-Thermal collectors for residential application in Bangkok, *Energies* **5**, 2012, 1229–1244.

[44] X. Wu, G. Gong and C. Wang, Experiment and performance analysis of amorphous silicon solar PV-thermal hybrid system, *Taiyangneng Xuebao/Acta Energiae Solaris Sinica* **38** (2), 2017, 363–371.

[45] Jing Li, Xiao Ren, Weiqi Yuan, Zhaomeng Li, Gang Pei, Yuehong Su, et al., Experimental study on a novel photovoltaic thermal system using amorphous silicon cells deposited on stainless steel, *Energy* **159**, 2018, 786–798.

[46] Runsheng Tang and Tong Wu, Optimal tilt-angles for solar collectors used in China, *Appl Energy* **79**, 2004, 239–248.

[47] Chao Guo, Jie Ji, Wei Sun, Jinwei Ma, Wei He and Yanqiu Wang, Numerical simulation and experimental validation of tri-functional photovoltaic/thermal solar collector, *Energy* **87**, 2015, 470–480.

[48] J.A. Duffie and W.A. Beckman, Solar engineering of thermal processes (4th ed.), 2013, John Wiley & Sons Inc.

[49] T.L. Bergman, F.P. Incropera, D.P. DeWitt and A.S. Lavine, Fundamentals of heat and mass transfer, 2011, John Wiley & Sons.

[50] ANSI/ASHRAE 93-2010 Methods of testing to determine the thermal performance of solar collectors. New York: ASHRAE; 2010.

[51] D.L. Staebler and C.R. Wronski, Reversible conductivity changes in discharge-produced amorphous Si, *Appl Phys Lett* **31**, 1977, 292–294.

[52] M. Nikolaeva, R.P. Kenny, E. Dunlop and M. Pravettoni, Seasonal variations on energy yield of a-Si, hybrid, and crystalline Si PV modules, *Prog Photovolt Res Appl* **18**, 2010, 311–320.

[53] A. Virtuani and L. Fanni, Seasonal power fluctuations of amorphous silicon thin-film solar modules: distinguishing between different contributions, *Prog Photovolt Res Appl* **22**, 2014, 208–217.

[54] <https://www.energyplus.net/weather-location/asia_wmo_region_2/CHN//CHN_Anhui.Hefei.583210_CSWD>.

[55] R.W. Moss, P. Henshall, F. Arya, G.S.F. Shire, T. Hyde and P.C. Eames, Performance and operational effectiveness of evacuated flat plate solar collectors compared with conventional thermal, PVT and PV panels, *Appl Energy* **216**, 2018, 588–601.

[56] Deepali Atheaya, Arvind Tiwari, I.M. Al-Helal and G.N. Tiwari, Performance evaluation of inverted absorber photovoltaic thermal compound parabolic concentrator (PVT-CPC): constant flow rate mode, *Appl Energy* **167**, 2016, 70–79.

Footnotes

[1] For interpretation of color in Fig. 4, the reader is referred to the web version of this article.

Highlights

- Design and construction of a novel standard sized a-Si PV/T system are introduced.
- Long-term experimental results of the system at medium temperature are presented.
- Distributed parameter model is established and validated by experiments.
- An insight to heat transfer and power generation is provided.
- The technical and thermodynamic feasibility at medium temperature is demonstrated.

Queries and Answers

Query: Your article is registered as a regular item and is being processed for inclusion in a regular issue of the journal. If this is NOT correct and your article belongs to a Special Issue/Collection please contact J.Shanmugam@elsevier.com immediately prior to returning your corrections.
Answer: Yes

Query: The author names have been tagged as given names and surnames (surnames are highlighted in teal color). Please confirm if they have been identified correctly.
Answer: Yes

Query: Please note that Fig. 4 will appear in B/W in print and color in the web version. Based on this, please approve the footnote 1 which explains this.

Answer: I understand.

Query: Have we correctly interpreted the following funding source(s) and country names you cited in your article: Bureau of International Cooperation, Chinese Academy of Sciences, China; National Science Foundation of China, China; Marie Curie, United Kingdom; ? /

Answer: Yes